

## Bulk O<sub>2</sub> formation and Mg displacement explain O-redox in Na<sub>0.67</sub>Mn<sub>0.72</sub>Mg<sub>0.28</sub>O<sub>2</sub>

Edouard Boivin<sup>1,3</sup>, Robert A. House<sup>1,2,3</sup>, Miguel A. Pérez-Osorio<sup>1,2,3</sup>, John-Joseph Marie<sup>1,2,3</sup>, Urmimala Maitra<sup>1</sup>, Gregory J. Rees<sup>1,2,3</sup>, Peter G. Bruce<sup>1,2,3,Δ,\*</sup>

1. Departments of Materials and Chemistry, University of Oxford, Parks Road, OX3 1PH, United Kingdom.
2. The Faraday Institution, Quad One, Becquerel Avenue, Harwell Campus, Didcot, OX11 0RA, United Kingdom
3. The Henry Royce Institute, Oxford, Parks Road, OX1 3PH, United Kingdom

Δ Lead contact

\*Corresponding author: peter.bruce@materials.ox.ac.uk

### Summary

O-redox in compounds with Li on the transition metal layers (TML) has recently been attributed to the formation of molecular O<sub>2</sub> on charge, trapped in the lattice. Here we show that a similar process occurs for P2-Na<sub>0.67</sub>[Mn<sub>0.72</sub>Mg<sub>0.28</sub>]O<sub>2</sub>, which contains Mg<sup>2+</sup> on the TML. The molecular O<sub>2</sub> is identified by high resolution RIXS and quantified by magnetometry showing that it equates to the charge passed. This O<sub>2</sub> is trapped in voids which are formed by Mg<sup>2+</sup> out-of-plane displacement and Mn<sup>4+</sup> in-plane disordering and is then reduced on discharge associated with a large voltage hysteresis. In contrast to compounds containing Li<sup>+</sup> in the TML, in which the honeycomb ordering and the high voltage plateau are irreversibly lost after the 1<sup>st</sup> cycle, in P2-Na<sub>0.67</sub>[Mn<sub>0.72</sub>Mg<sub>0.28</sub>]O<sub>2</sub>, the plateau reappears partially on the 2<sup>nd</sup> charge due to the partial reversibility of Mn in-plane and Mg out-of-plane migration and the local reformation of the honeycomb ordering.

### Introduction

Alkali metal (AM) intercalation compounds based on layered transition metal (TM) oxides and containing Li in the TM layers, such as Li<sub>1.2</sub>Ni<sub>0.13</sub>Mn<sub>0.54</sub>Co<sub>0.13</sub>O<sub>2</sub>, exhibit capacity in addition to that associated with TM redox by invoking redox reactions on the O<sup>2-</sup> ions.<sup>1–3</sup> The coordination of the O<sup>2-</sup> ions by alkali ions in the transition metal as well as the alkali metal layers raises the energy of the O2p states rendering them accessible to oxidation within the voltage stability window of common organic electrolytes.<sup>4</sup> The nature of the oxidized oxygen has been widely debated with localized holes (O<sup>•</sup>), peroxo (O<sub>2</sub><sup>2-</sup>), peroxo-like (O<sub>2</sub><sup>n-</sup>) and superoxo (O<sub>2</sub><sup>-</sup>) species being proposed.<sup>1,5–7</sup> It has been shown recently that in such compounds, specifically O3-Li<sub>1.2</sub>Ni<sub>0.13</sub>Mn<sub>0.54</sub>Co<sub>0.13</sub>O<sub>2</sub> and P2-Na<sub>0.75</sub>Li<sub>0.25</sub>Mn<sub>0.75</sub>O<sub>2</sub>, the oxidation of O<sup>2-</sup> results in O<sup>•</sup> disproportionation forming O<sub>2</sub> molecules, which are physically trapped in voids within the bulk of the particles formed by in-plane TM migration.<sup>8,9</sup> This O<sub>2</sub> is then reduced on discharge, explaining the 1<sup>st</sup> cycle voltage hysteresis systematically observed. Investigation of P2-Na<sub>0.67</sub>Mn<sub>0.72</sub>Mg<sub>0.28</sub>O<sub>2</sub> and more recently P2-Na<sub>0.67</sub>Mn<sub>0.78</sub>Zn<sub>0.22</sub>O<sub>2</sub> has shown that O-redox is not restricted to alkali-rich compounds, but can be activated in compounds with divalent ions, such as Mg<sup>2+</sup> or

$\text{Zn}^{2+}$ .<sup>10,11</sup> However, the nature of oxidized oxygen in the bulk and the persistence of charging plateaus as well as the voltage hysteresis in these materials remains to be understood.  $\text{P2-Na}_{0.67}\text{Mn}_{0.72}\text{Mg}_{0.28}\text{O}_2$  is a useful material to study this question as it shows almost pure O-redox, no  $\text{O}_2$  loss from the lattice and Mn is the only TM.

Here, we show that molecular  $\text{O}_2$  physically trapped in the bulk of particles is the primary form of oxidized oxygen species formed on charging  $\text{P2-Na}_{0.67}\text{Mn}_{0.72}\text{Mg}_{0.28}\text{O}_2$ . The  $\text{O}_2$  was identified using high resolution O K-edge RIXS and quantified by magnetometry, which showed close agreement with the charge passed across the plateau corresponding to the O-redox process.  $\text{Mg}^{2+}$  is displaced from the transition metal layers into the alkali metal layers, as also observed for  $\text{Zn}^{2+}$  upon charging  $\text{P2-Na}_{0.67}\text{Mn}_{0.78}\text{Zn}_{0.22}\text{O}_2$ .<sup>11</sup> The  $\text{Mg}^{2+}$  migrates to tetrahedral and octahedral sites in the AM layer, with half the  $\text{Mg}^{2+}$  in each site. The vacancies generated in the TM layer allow in-plane disorder of  $\text{Mn}^{4+}$ . The in-plane Mn/ $\square$  redistribution, confirmed by n-PDF, converges into stable vacancy cluster voids that can accommodate O-O dimers with a bond length of 1.23 Å, characteristic of molecular oxygen. In contrast to compounds with Li in the TM layers where the honeycomb ordering and the high voltage plateau are irreversibly lost on the first cycle,<sup>2,5,12</sup> in  $\text{P2-Na}_{0.67}\text{Mn}_{0.72}\text{Mg}_{0.28}\text{O}_2$ , the initial honeycomb ordering, observed at long range in the pristine material, is partially reformed at the local scale on discharge. After several cycles, the high voltage plateau is no longer observed indicating complete loss of honeycomb ordering.

## Results

### Structure and electrochemical properties

Time-of-Flight Neutron Powder Diffraction (TOF-NPD) data were used to refine the structure of  $\text{P2-Na}_{0.67}\text{Mn}_{0.72}\text{Mg}_{0.28}\text{O}_2$  using the  $\text{P6}_3/\text{mcm}$  space group, which captures the honeycomb ordering of the Mg/Mn within the TM layer.  $\text{Na}_{0.67}\text{Mn}_{0.72}\text{Mg}_{0.28}\text{O}_2$  was the closest composition to the ideal honeycomb (*i.e.*  $\text{Na}_{2/3}\text{Mn}_{2/3}\text{Mg}_{1/3}\text{O}_2$ ) that we could prepare as a pure phase. The difference is accounted for in the structure by some occupancy of Mn in the Mg sites (**Figure S1** and **Table S1**). The galvanostatic cycling of  $\text{Na}_{0.67}\text{Mn}_{0.72}\text{Mg}_{0.28}\text{O}_2$  is shown in **Figure 1**. The initial sloped region corresponds to the small amount of  $\text{Mn}^{3+}/\text{Mn}^{4+}$  redox activity and accounts for the extraction of  $\sim 0.14 \text{ Na}^+$ , while the high voltage plateau observed upon further  $\text{Na}^+$  extraction is charge compensated through O-redox rather than O-loss from the lattice. Indeed, the lack of  $\text{O}_2$  gas loss from the particle surface for this material has been shown previously.<sup>10</sup> The plateau is not preserved upon discharge and instead a sloping profile is seen with a large voltage hysteresis. This behavior is common to most O-redox cathode materials and has been assigned previously to formation of molecular  $\text{O}_2$  trapped in the bulk of particles.<sup>8,9</sup> However, the presence of a shortened plateau during subsequent charge of such a honeycomb ordered compound

is a feature observed only upon cycling of  $\text{P2-Na}_{2/3}\text{Mn}_{0.72}\text{Mg}_{0.28}\text{O}_2$ ,  $\text{P3-Na}_{0.67}\text{Mn}_{0.67}\text{Mg}_{0.33}\text{O}_2$  and  $\text{P2-Na}_{0.67}\text{Mn}_{0.78}\text{Zn}_{0.22}\text{O}_2$ .<sup>13,14</sup>

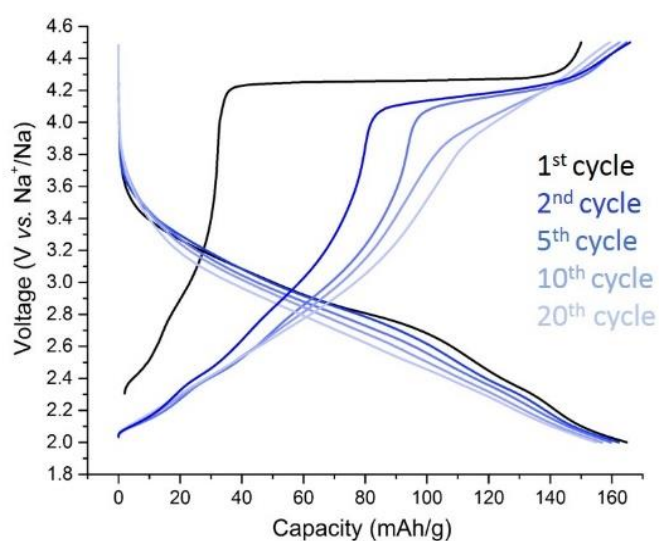


**Figure 1: Electrochemical properties.** Galvanostatic cycling of  $\text{P2-Na}_{0.67}\text{Mn}_{0.72}\text{Mg}_{0.28}\text{O}_2$  showing that the high voltage plateau is retained for several cycles although progressively lost.

#### Identification and quantification of bulk molecular $\text{O}_2$

In order to identify the nature of oxidized oxygen formed in  $\text{Na}_{0.67}\text{Mg}_{0.28}\text{Mn}_{0.72}\text{O}_2$  and in particular to see whether  $\text{O}_2$  is formed and trapped in the bulk, O K-edge XAS and RIXS measurements were carried out (**Figure 2**).

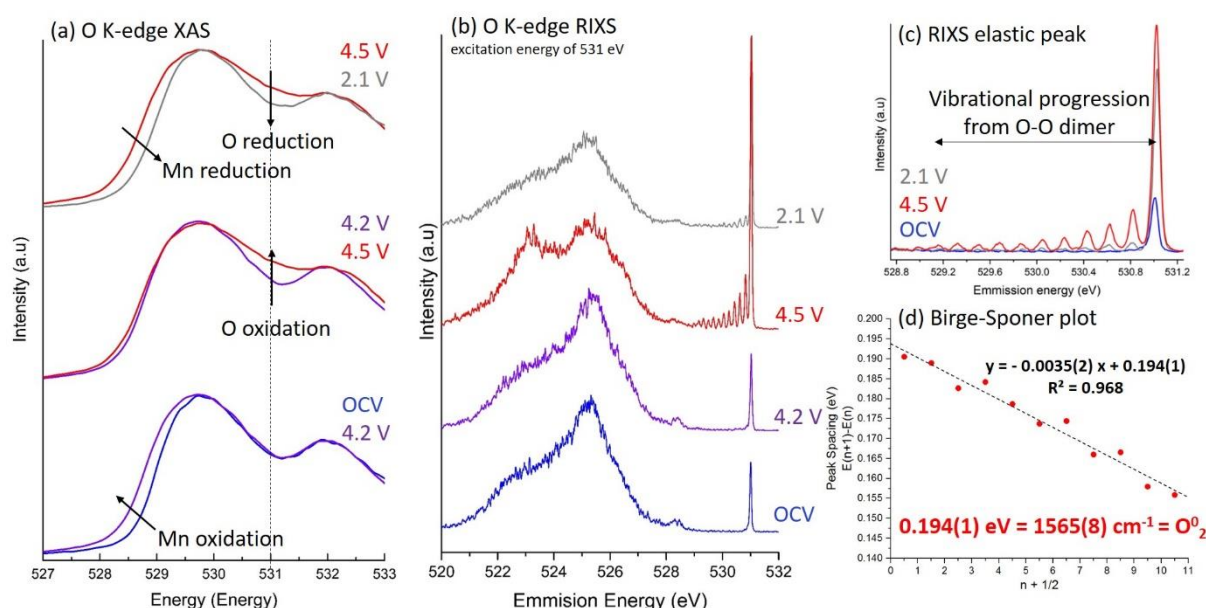


**Figure 2: Identification of molecular  $\text{O}_2$ .** (a) O K-edge XAS and (b) O K-edge RIXS collected at an excitation energy of 531 eV for  $\text{P2-Na}_{0.67}\text{Mn}_{0.72}\text{Mg}_{0.28}\text{O}_2$  at OCV (blue), 4.2 V (purple), 4.5 V (red) and following discharge to 2.1 V (grey). An enlargement of the elastic peak is shown in (c). The Birge-Sponer plot (d) of the fully charged material reveals that the peak spacing near the elastic peak corresponds to a fundamental vibrational energy of 0.194(1) eV which is typical for molecular  $\text{O}_2$ .

O K-edge XAS and high resolution RIXS spectra for pristine and cycled  $\text{Na}_{0.67}\text{Mn}_{0.72}\text{Mg}_{0.28}\text{O}_2$  are shown in **Figure 2a** and **Figure 2b** respectively. Charging to the beginning of the plateau (i.e. 4.2 V vs  $\text{Na}^+/\text{Na}$ ) generates electron hole states in hybridized Mn-O orbitals of primarily Mn character and associated with Mn redox, observed between 528 and 529 eV in XAS, while oxide oxidation across the high voltage plateau creates electron hole states at 531 eV.<sup>10</sup> The RIXS spectra collected at this excitation energy reveal new oxygen valence states (centered at 523 eV) in addition to a strong increase of the elastic peak, in good agreement with that reported previously for this system.<sup>10</sup> The higher resolution RIXS that we employed here compared to past studies reveals the underlying fine structure of the “elastic” contribution (**Figure 2c**), which is composed of a succession of energy loss peaks similar to that observed for charged  $\text{O3-Li}_{1.2}\text{Ni}_{0.13}\text{Mn}_{0.54}\text{Co}_{0.13}\text{O}_2$  and  $\text{P2-Na}_{0.75}\text{Li}_{0.25}\text{Mn}_{0.75}\text{O}_2$  as well as  $\text{O}_2$  gas.<sup>8,9,15</sup> They are associated with transitions to different vibrational energy levels of an O-O dimer and the peak spacing indicates the nature of this O-O dimer.<sup>16</sup> The extrapolation of the Birge-Sponer plot, shown in **Figure 2d**, at  $n=0$  gives a fundamental vibrational energy of 0.194(1) eV which corresponds to  $1565(8) \text{ cm}^{-1}$ , consistent with that of molecular  $\text{O}_2$  ( $\sim 1556 \text{ cm}^{-1}$ ).<sup>17</sup> This wavenumber value is very different from the vibrational frequency of any negatively charged oxygen dimer (either  $\text{O}_2^{2-}$  at ca.  $750 \text{ cm}^{-1}$ ,  $\text{O}_2^-$  at ca.  $1100 \text{ cm}^{-1}$  or in between for  $\text{O}_2^{n-}$ ).<sup>17</sup> This is in accord with the absence of a signal in the  $700\text{--}1200 \text{ cm}^{-1}$  range in the charged state of  $\text{Na}_{0.67}\text{Mn}_{0.72}\text{Mg}_{0.28}\text{O}_2$  measured by bulk sensitive Raman spectroscopy.<sup>10</sup> Elsewhere, indications of peroxo-like species seen using surface enhanced Raman (SERS) are most likely to arise from surface-localised phenomena (i.e. CEI formation

or surface decomposition products)<sup>18,19</sup> that might surface bias bulk sensitive Raman. The RIXS data in the discharged state (*i.e.* 2.1 V, the composition of the pristine material) reveals the persistence of a much weaker progression of energy loss peaks associated with the elastic peak, indicating that the O<sub>2</sub> is significantly reduced on discharge but not entirely and hence that some Mn<sup>4+</sup> starts to be reduced before all the O<sub>2</sub> is reduced completely to O<sup>2-</sup> consistent with previous XANES studies.<sup>10</sup>

While RIXS presents evidence for O<sub>2</sub> molecules trapped in the bulk of the particles, it is difficult to quantify the amount of O<sub>2</sub> and hence to show that it accords with the charge passed. Quantification of the O<sub>2</sub> can be achieved by exploiting its paramagnetism with magnetometry measurements, which also possess the advantage of being free from any possibility of beam damage. The formation of molecular oxygen O<sub>2</sub>, localized holes O<sup>•</sup>, peroxo O<sub>2</sub><sup>2-</sup>, peroxo-like O<sub>2</sub><sup>n-</sup> or superoxo O<sub>2</sub><sup>-</sup> species would generate unpaired electrons to different extents for the same degree of oxidation, *i.e.* Na removed (as represented by the dash lines at **Figure 3**). As an example, the exclusive formation of peroxo species across the high voltage plateau, would not lead to an increase of the Curie constant, O<sub>2</sub><sup>2-</sup> being diamagnetic. Also, O<sup>•</sup> and O<sub>2</sub>, which nominally have the same number of unpaired electrons per O, can be distinguished since there would need to be twice as many of the former than the latter to account for the same degree of oxidation. The experimental data shown in **Figure 3** and summarized in the **Table S2** demonstrate the gradual rise of the Curie constant along with the activation of O-redox until 1.458(9) cm<sup>3</sup>.mol<sup>-1</sup> at the charged state. This value is in good agreement with charge compensation occurring predominantly via the O<sup>2-</sup>/O<sub>2</sub> redox couple ( $C_{th}=1.453$  cm<sup>3</sup>.mol<sup>-1</sup>). The quantity of charge passed based on the amount of O<sub>2</sub> estimated from magnetometry is 0.432 ± 0.036 electrons which is consistent with 0.41 electrons exchanged across the high voltage plateau and corresponds to approximately 10% of the oxide ions being in the form of O<sub>2</sub>. Note that Na<sub>0.67</sub>Mn<sub>0.72</sub>Mg<sub>0.78</sub>O<sub>2</sub> provides a good system with which to quantify O<sub>2</sub> with magnetometry since spin counting is simple with Na<sup>+</sup>, Mg<sup>2+</sup> and Mn<sup>4+</sup> as the only cations.

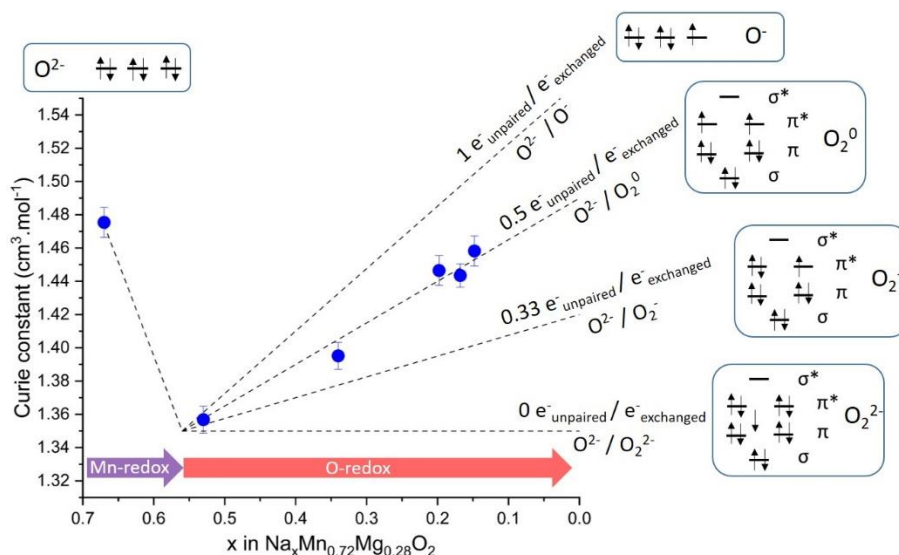


**Figure 3: Quantification of molecular  $O_2$ .** Curie constant as a function of the Na content in  $Na_xMn_{0.72}Mg_{0.28}O_2$  measured experimentally (blue dots) and predicted based on different hypothesis for O-redox couples involved:  $O^{2-}/O^-$  (localized holes),  $O^{2-}/O_2^0$  (molecular oxygen),  $O^{2-}/O_2^{2-}$  (peroxo) and  $O^{2-}/O_2^-$  (superoxo) represented as black dash lines. The experimental data fit well with the number of unpaired electrons expected for the exclusive formation of molecular  $O_2$  upon  $O^{2-}$  oxidation. Details for the estimation of the error bar are provided in Table S2.

### Long range honeycomb ordering

In materials with Li in the TM layers, Li extraction and in-plane TM disordering on charging forms voids that accommodate  $O_2$  and the TM disorder is associated with the irreversible loss of the honeycomb superstructure.<sup>8,9</sup> In order to probe the evolution of the long range ordering within the TM layer in  $P2-Na_{0.67}Mg_{0.28}Mn_{0.72}O_2$ , operando PXRD was employed (**Figure 4**). On charging, the continuous shift in the PXRD peak positions in the initial sloped region of the voltage curve is in accord with this being a single-phase reaction. The reaction associated with the high voltage plateau corresponds to the two-phase structural transition from a honeycomb ordered P2 phase to an O2 phase, in good agreement with results reported previously.<sup>10,20</sup> Not all the Na is removed at the end of charge, commensurate with the persistence of peaks associated with some P2 phase. It is noteworthy that at the end of subsequent discharge the honeycomb superstructure peak is again present, although reduced in magnitude compared to that observed in the pristine material.

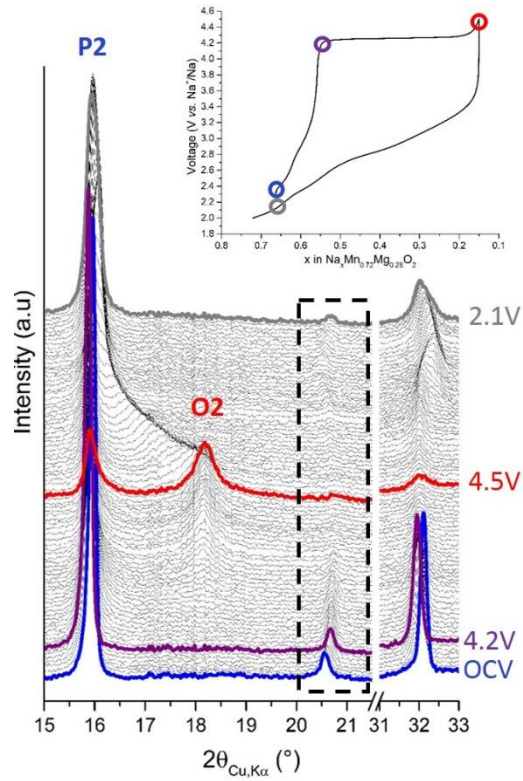


**Figure 4: Average structure evolution upon cycling.** operando PXRD during 1<sup>st</sup> galvanostatic cycling of P2- $\text{Na}_{0.67}\text{Mn}_{0.72}\text{Mg}_{0.28}\text{O}_2$  (shown in inset). The high voltage plateau associated to the  $\text{O}^{2-}$  oxidation corresponds to a two- phase reaction between the P2 and an O2 phase, while the discharge is associated with a continuous evolution back to a P2 structure. The honeycomb superstructure peak (shown in the box) is present at the end of discharge although reduced in magnitude.

#### Reversible Mg out-of-plane migration

In order to form O<sub>2</sub> trapped within the particles, structural changes have to occur. To investigate the structural changes on charging, Mg and Mn K-edge EXAFS were employed.

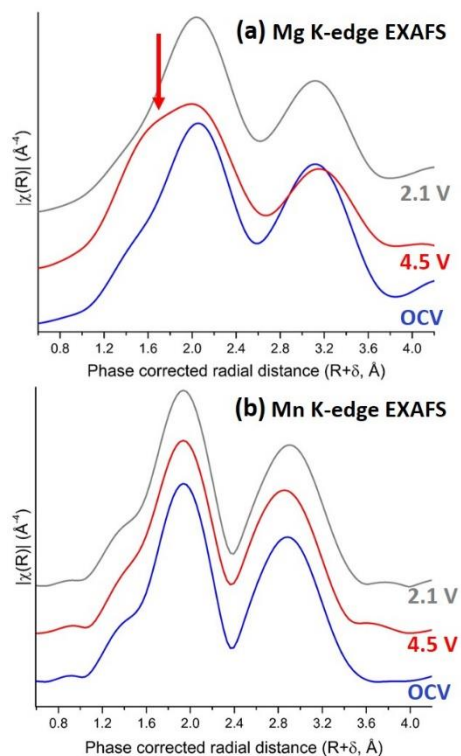


**Figure 5: Reversible Mg out-of-plane migration.** Mg K-edge EXAFS (a) and Mn K-edge EXAFS (b) data collected at OCV, charged to 4.5 V and discharged to 2.1 V. The appearance of a shoulder at low radial distance in the 1<sup>st</sup> shell Mg K-edge EXAFS at the charged state (highlighted by the red arrow) is consistent with Mg occupancy of a new tetrahedral site while the Mn environment is hardly changed. The fit of the Mg EXAFS at 4.5V is provided in Figure S3 and the corresponding fitting parameters in Table S3.

Except for a tiny shortening of the Mn-O distance upon charge, the Mn K-edge EXAFS does not show any significant change in the first coordination shell on cycling. In contrast, in the Mg K-edge EXAFS, a shoulder arises at low radial distance (see red arrow in the **Figure 5a**) indicating that Mg occupies a new site in the charged state. The short Mg-O bond (*ca.* 1.8  $\text{\AA}$ ) is in accord with that of Mg in a tetrahedral site (as seen for instance in the spinel  $\text{MgM}_2\text{O}_4$  with  $\text{M} = \text{Al, Cr, Mn or Fe}$ )<sup>21</sup>. In the O2 structure of the charged material, two distinct tetrahedral sites are accessible, either in the TM layer or in the AM layer. However, migration of Mg from its original octahedral site towards the tetrahedral site of the TM layer would imply face sharing with 2  $\text{MnO}_6$  octahedra with an approximate Mg-Mn distance of 2.5  $\text{\AA}$ , which is unlikely and clearly not seen either in the Mg K-edge or the Mn K-edge EXAFS. Therefore, in the charged state, Mg migrates into tetrahedral sites in the AM layer as also observed in the charged  $\text{P3-Na}_{2/3}\text{Mn}_{2/3}\text{Mg}_{1/3}\text{O}_2$ <sup>13</sup> and for  $\text{Zn}^{2+}$  in charged  $\text{P2-Na}_{0.67}\text{Mn}_{0.78}\text{Zn}_{0.22}\text{O}_2$ .<sup>11</sup> Octahedral vacancies now surround Mn in the TM layer enabling Mn in-plane disordering. Mg is also likely to disorder within the AM layer to avoid face sharing along the c-axis with the Mn ions that

migrate in-plane into the sites vacated by  $\text{Mg}^{2+}$ . The persistence of a peak in the Mg EXAFS corresponding to a Mg-O distance of 2.05 Å, indicates that some of the Mg also occupies octahedral sites in the AM layers, as discussed in the following section. At the end of the discharge, when the composition has returned to the original value, the EXAFS spectra of the Mn and Mg K-edges are very similar to those observed for the pristine material, indicating that Mg returns to octahedral sites in the TM layer.

### **Mn in-plane migration and Mg displacement driven by bulk $\text{O}_2$ formation**

To explore the  $\text{Mn}/\square$  ( $\square$  = cation vacancy) disorder formed on charging, DFT and n-PDF have been employed and are summarized in **Figure 6**, **Figure 7** and **Figure S2**. The fully charged structure composed of  $[\square_{2/3}\text{Mg}_{1/3}]\text{O}_2$  (AM) and  $[\text{Mn}_{2/3}\square_{1/3}]\text{O}_2$  (TM) layers stacked in a O2 sequence was employed as the DFT model to explore the  $\text{Mn}/\square$  and  $\text{Mg}/\square$  distribution within the TM and AM layers respectively. The ideal honeycomb structure of  $\text{Mg}_{1/3}\text{Mn}_{2/3}\text{O}_2$  was used for DFT to ensure a tractable cell size for the calculations, as employed previously.<sup>10</sup> Although, most of the  $\text{Mn}/\square$  distributions explored gave rise to energies comparable to  $k_B T$ , one  $\text{Mn}/\square$  configuration leads to a large stabilization (-410 meV/f.u. see **Figure S2**). This structure involves clusters of 4 vacancies, as shown in **Figure 6e**, and the formation of O-O dimers with a bond length of 1.23 Å, as observed for molecular oxygen (1.21 Å for  $\text{O}_2$  vs. 1.28 Å for  $\text{O}_2^-$ , 1.48 Å for  $\text{O}_2^{2-}$  or in the 1.4-2.5 Å range for  $\text{O}_2^n$ ).<sup>17</sup> This 4 vacancy cluster with two  $\text{O}_2$  molecules trapped inside is similar to the moiety recently identified in charged  $\text{Li}_{1.2}\text{Ni}_{0.13}\text{Mn}_{0.54}\text{Co}_{0.13}\text{O}_2$ .<sup>9</sup> Moreover, within the AM layer of the O2 structure, the DFT studies indicate that Mg is distributed between tetrahedral sites (sharing a face with a vacant octahedral site in the TM layer) and the octahedral sites of the O2-structure (sharing 3 edges with  $\text{Mn}/\square$  octahedra of the TM layer above and a face with a vacancy of the TM layer below). Fitting of the Mg K-edge EXAFS shows that approximately 50% of the Mg in the O2 phase is found in the tetrahedral sites and 50% in the octahedral sites, **Figure S3** and **Table S3**, in line with the lowest energy configuration found by DFT.

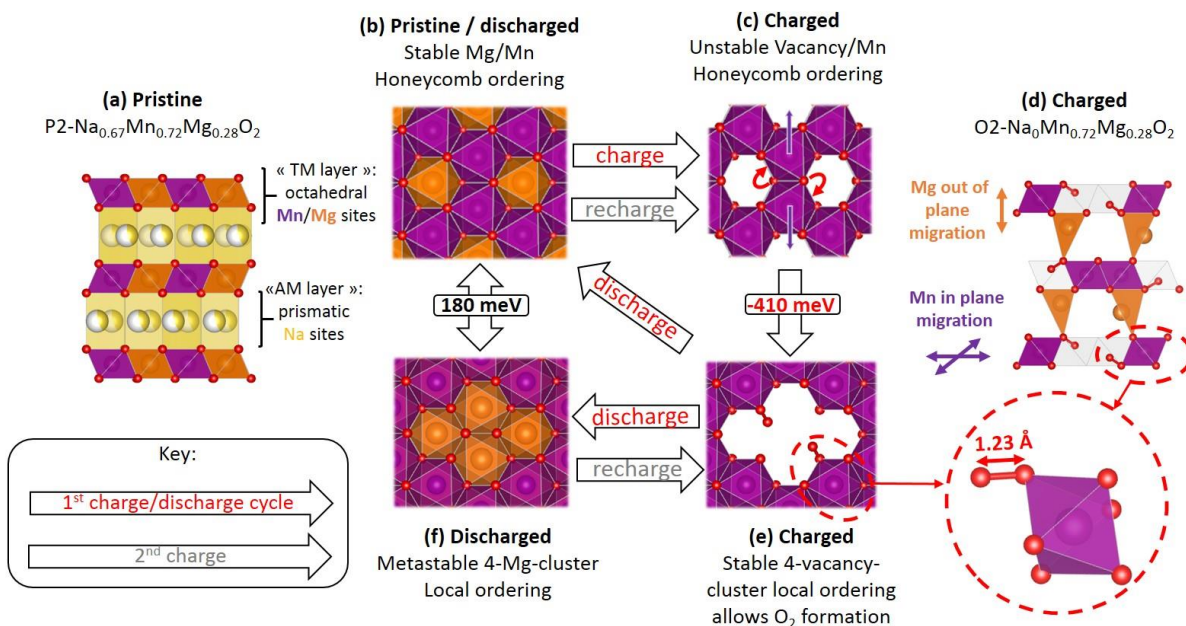


**Figure 6: The molecular  $\text{O}_2$  formation mechanism.** (a)  $P2\text{-Na}_{2/3}\text{Mn}_{2/3}\text{Mg}_{1/3}\text{O}_2$  used for DFT modelling viewed along the  $[110]$  direction and (b) TM layer viewed along  $[001]$  where Mn purple, Mg orange, Na yellow and O red. Upon charge (top row), the Mg out of plane migration generates vacancies in the TM layer (c, d). The unstable honeycomb ordering of Mn and vacancies (c) transforms, by Mn in-plane disordering, into a stable 4-vacancy-cluster that accommodates  $\text{O}_2$  molecules (d and e) and provides a stabilization of 410 meV/f.u. The honeycomb ordering of Mg/Mn in the discharged state is thermodynamically favored while the 4-Mg-cluster (f) is metastable (+180 meV/f.u.). Arrows with red text show 1<sup>st</sup> charge/discharge pathways and those with grey 2<sup>nd</sup> charge. The energy of all DFT models explored as well as the partial density of state of selected models are provided in the Figure S2.

On discharge, when  $\text{Mg}^{2+}$  returns to the TM layers, two options for Mn/Mg distribution are possible: either  $\text{Mg}^{2+}$  occupies the octahedral sites in the TM layer within the vacancy cluster (similar to that observed for  $\text{Li}^+$  returning to the TM layer in  $\text{Na}_{0.75}\text{Mn}_{0.75}\text{Li}_{0.25}\text{O}_2$ )<sup>8</sup>, **Figure 6f** or the Mn/Mg honeycomb ordering is recovered implying reversibility of the in-plane Mn migration (**Figure 6b**). Both possibilities have been explored with DFT. As expected, when Mg and Mn occupy the TM layer, the honeycomb ordering is the most stable configuration in the discharge state (*i.e.* the composition of the pristine material). In comparison the Mg in the cluster configuration is metastable by 180 meV/f.u. (**Figure S2**).

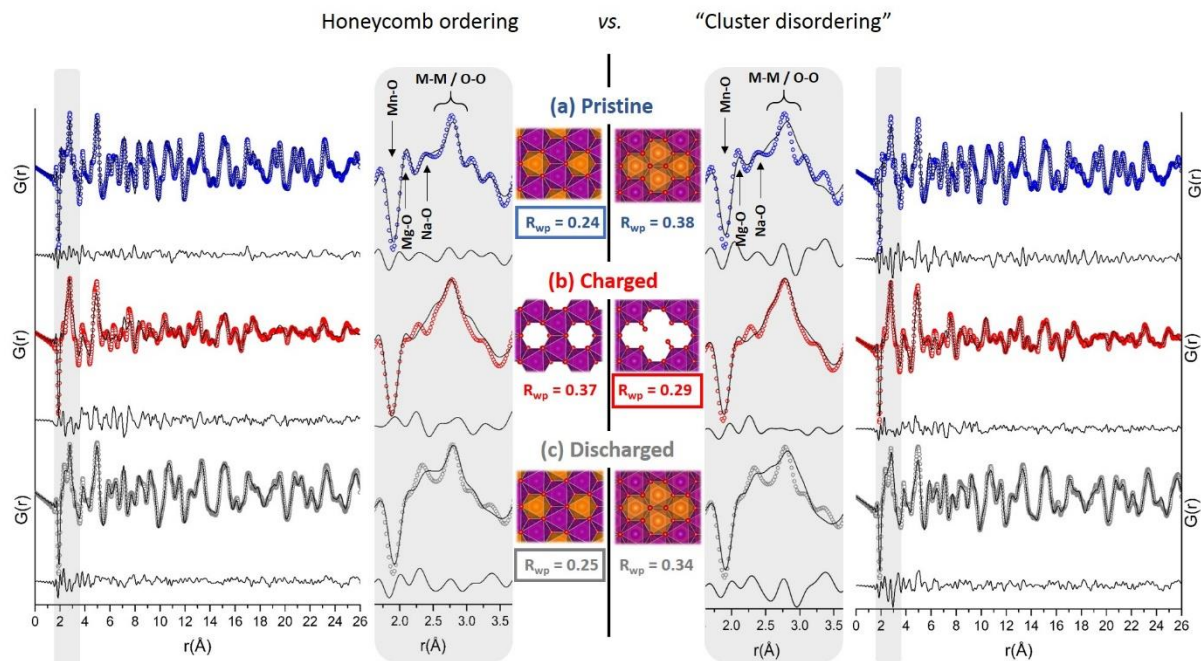


**Figure 7: Local structure evolution upon cycling.** fits of the n-PDF data for (a) pristine, (b) charged and (c) discharged materials. In inset an enlargement of the short-range region (1-4 Å) highlighted in grey. The relaxed DFT structures (illustrated in inset, Mg is in orange, Mn in purple and O in red) have been used as starting models for the fits of n-PDF data. Honeycomb ordering and cluster disordering are systematically compared at each state of charge. Based on the agreement factors, it is shown that the honeycomb ordering is lost on charge with vacancy clusters showing a better fit and reformed at the local scale on discharge.

To probe the formation of the vacancy cluster voids experimentally and thus corroborate the DFT model, n-PDF was employed. The models obtained from DFT were used as a starting point for the analysis (as described in experimental section), see **Figure 7**. For the pristine material, the fit of the n-PDF data using the DFT model gives similar agreement factors to those using the long range structure determined by diffraction ( $R_{wp}=0.24$  vs.  $R_{wp}=0.22$ ). This indicates that, despite a composition slightly different to the one determined by NPD (*i.e.*  $\text{Na}_{0.67}\text{Mn}_{0.67}\text{Mg}_{0.33}\text{O}_2$  vs.  $\text{Na}_{0.67}\text{Mn}_{0.72}\text{Mg}_{0.28}\text{O}_2$ ), the relaxed DFT models can be used to fit the n-PDF patterns. Since, at the end of charge the conversion from  $\text{P2-}[\text{Na}_{0.56}][\text{Mn}_{0.72}\text{Mg}_{0.28}]\text{O}_2$  to  $\text{O2-}[\square_{0.67}\text{Mg}_{0.28}][\text{Mn}_{0.72}\square_{0.28}]\text{O}_2$  is incomplete, a two phases refinement was employed fixing the P2/O2 ratio to that obtained experimentally based on the amount of the  $\text{Na}^+$  electrochemically extracted (see experimental section). For the  $\text{O2-}[\square_{0.67}\text{Mg}_{0.33}][\text{Mn}_{0.67}\square_{0.33}]\text{O}_2$  phase, two models were explored: Mn/ $\square$  clusters or a Mn/ $\square$  honeycomb ordering. The ordering of the Mn ions into 4-vacancy-clusters provides a significantly better agreement factor than Mn remaining in the sites occupied in the pristine material ( $R_{wp}=0.29$  vs.  $R_{wp}=0.37$ , see **Figure 7b**). The n-PDF data confirms that the honeycomb ordering is lost even at the short range on charging and hence that the decrease of the superstructure peak intensity seen on charge by operando PXRD (see **Figure 4**) is due to the loss of honeycomb ordering rather than the disruption of the coherence arising from stacking faults. On

discharge, the honeycomb ordering of Mg/Mn provides a better agreement with the n-PDF data than Mg/Mn clusters ( $R_{wp}=0.25$  for honeycomb vs.  $R_{wp}=0.34$  for 4-Mg-cluster, see **Figure 7c**). Therefore, the n-PDF data show that the honeycomb ordering present in the pristine material is lost on charge then reformed at the local scale on the first discharge in accord with the formation and annihilation of the 4-vacancy-clusters on charge and discharge.

## Discussion

Previous studies of  $P2\text{-Na}_{0.67}\text{Mn}_{0.72}\text{Mg}_{0.28}\text{O}_2$  have employed only standard RIXS spectroscopy.<sup>10,22</sup> While such spectroscopy can identify that oxidation is taking place on the  $\text{O}^{2-}$ , it cannot identify the species formed, molecular  $\text{O}_2$ , something that is possible with high resolution RIXS used here. Furthermore,  $P2\text{-Na}_{0.67}\text{Mn}_{0.72}\text{Mg}_{0.28}\text{O}_2$  permits investigation of O-redox by magnetometry as there is only one other redox active cation. Magnetometry has enabled the quantification of  $\text{O}_2$  trapped in the particles and shows that this is in close agreement with the charge passed, providing valuable confirmation of the assignment of O-redox to  $\text{O}_2$  formation. The O-redox behavior of  $P2\text{-Na}_{0.67}\text{Mn}_{0.72}\text{Mg}_{0.28}\text{O}_2$  exhibits similarities but also important differences compared with compounds possessing Li in the TM layer, such as  $\text{O3-Li}_{1.2}\text{Ni}_{0.13}\text{Mn}_{0.54}\text{Co}_{0.13}\text{O}_2$  and  $P2\text{-Na}_{0.75}\text{Li}_{0.25}\text{Mn}_{0.75}\text{O}_2$ . In terms of similarities, alkali extraction is charge compensated by oxidation of  $\text{O}^{2-}$  to form  $\text{O}_2$  trapped in cation vacancy cluster voids in the TM layer generated by in-plane TM disordering, the  $\text{O}_2$  being reduced back to  $\text{O}^{2-}$  on discharge. The similarity in bond length between trapped and gaseous  $\text{O}_2$  indicates the  $\text{O}_2$  molecules are physically confined with relatively little chemical interaction with their surroundings. Previous  $^{17}\text{O}$  MAS NMR measurements have suggested that the trapped  $\text{O}_2$  exists in a solid-like environment with lack of rotational motion. However, in contrast to  $\text{O3-Li}_{1.2}\text{Ni}_{0.13}\text{Mn}_{0.54}\text{Co}_{0.13}\text{O}_2$  and  $P2\text{-Na}_{0.75}\text{Li}_{0.25}\text{Mn}_{0.75}\text{O}_2$ , in which Li is removed from the TM layers on charge (either occupying the octahedral sites in the AM layer in the case of  $P2\text{-Na}_{0.75}\text{Li}_{0.25}\text{Mn}_{0.75}\text{O}_2$  or extracted from  $\text{O3-Li}_{1.2}\text{Ni}_{0.13}\text{Mn}_{0.54}\text{Co}_{0.13}\text{O}_2$ )<sup>8,9</sup>, for  $P2\text{-Na}_{2/3}\text{Mn}_{0.72}\text{Mg}_{0.28}\text{O}_2$  the  $\text{Mg}^{2+}$  ions are displaced from the TM layers into tetrahedral and octahedral sites of the AM layers then return to octahedral sites in TM layers on discharge. In a previous paper on  $P2\text{-Na}_{0.67}\text{Mn}_{0.72}\text{Mg}_{0.28}\text{O}_2$  we did not detect Mg displacement. Here we have used EXAFS and PDF data that provide a bulk average understanding of local structure, whereas the previous study used STEM which may not have shown obvious Mg displacement due to lack of alignment in the Mg columns.<sup>10</sup> The low and sloping voltage curve on the discharge following the 1<sup>st</sup> charge is similar to that seen for  $\text{O3-Li}_{1.2}\text{Ni}_{0.13}\text{Mn}_{0.54}\text{Co}_{0.13}\text{O}_2$  and  $P2\text{-Na}_{0.75}\text{Li}_{0.25}\text{Mn}_{0.75}\text{O}_2$ , consistent with  $\text{Mg}^{2+}$  repopulating the octahedral sites in the vacancy clusters as discharge proceeds. However, in contrast to  $\text{O3-Li}_{1.2}\text{Ni}_{0.13}\text{Mn}_{0.54}\text{Co}_{0.13}\text{O}_2$  and  $P2\text{-Na}_{0.75}\text{Li}_{0.25}\text{Mn}_{0.75}\text{O}_2$  cases, the n-PDF data at the end of discharge for  $P2\text{-Na}_{0.67}\text{Mn}_{0.72}\text{Mg}_{0.28}\text{O}_2$  and the presence of a plateau on the subsequent charge are all consistent with the reformation of honeycomb ordering. It is important to note that only *ca.* 70% of

the 1<sup>st</sup> charge plateau is observed on the 2<sup>nd</sup> charge, the rest is accompanied by a sloping curve, indicating that the honeycomb ordering is not completely reformed on the 1<sup>st</sup> discharge. The 2<sup>nd</sup> charge of P2-Na<sub>0.67</sub>Mn<sub>0.72</sub>Mg<sub>0.28</sub>O<sub>2</sub> can be viewed as a hybrid of the voltage curves seen for P2-Na<sub>0.75</sub>Li<sub>0.25</sub>Mn<sub>0.75</sub>O<sub>2</sub> on the 1<sup>st</sup> charge (plateau) and 2<sup>nd</sup> charge (sloping) in which the plateau is associated with loss of honeycomb ordering and the sloped region to the depopulation of the vacancy clusters by Li<sup>+</sup>. We therefore suggest that for P2-Na<sub>0.67</sub>Mn<sub>0.72</sub>Mg<sub>0.28</sub>O<sub>2</sub> during the 1<sup>st</sup> discharge, as Na re-enters the structure, Mg is displaced back into the TM layers partly into vacancy cluster sites but also into honeycomb sites which are reformed by reversing the Mn migration. The 2<sup>nd</sup> charge involves depopulation of Mg from the clusters and O<sub>2</sub> formation, giving rise to the sloping region of the charging curve - which also accounts for a minor contribution of the Mn<sup>3+</sup>/Mn<sup>4+</sup> redox as shown previously by quantitative XAS<sup>22,23</sup> - and loss of honeycomb, resulting in the 2<sup>nd</sup> charge plateau. This 2<sup>nd</sup> charge plateau is also observed in Na<sub>0.67</sub>Mn<sub>0.78</sub>Zn<sub>0.22</sub>O<sub>2</sub>, where tetrahedral Zn<sup>2+</sup> has also been identified at charged state. The reduced mobility of Mg<sup>2+</sup> and Zn<sup>2+</sup> ions which remain predominantly in the sites adjacent to their original octahedral site in the TM layer in the charged structure, may offer an explanation as to why the honeycomb ordering is partially reformed on discharge. Li on the other hand is much more mobile and can diffuse quickly to find an available vacancy cluster elsewhere in the TM layer. As shown recently, the O K-edge RIXS signature remains mostly unchanged at the 100<sup>th</sup> charge compared with 1<sup>st</sup> charge,<sup>22</sup> and hence, although the structural transition from vacancy cluster to honeycomb ordering is partly irreversible, the formation of molecular O<sub>2</sub> is almost fully reversible. Eventually, the honeycomb ordering of Mg is completely lost leading to the loss of the reordering phenomenon and the charging plateau over cycling. Further studies are required to understand the behaviour of O<sub>2</sub> trapped in voids over extensive cycling and especially its influence on the complex issues of voltage fade and capacity decay.

## Conclusion

High resolution RIXS spectroscopy demonstrates that O-redox in P2-Na<sub>0.67</sub>Mn<sub>0.72</sub>Mg<sub>0.28</sub>O<sub>2</sub> involves formation of molecular O<sub>2</sub> on charge, which is reduced back to O<sup>2-</sup> on subsequent discharge. The quantity of O<sub>2</sub> trapped in the structure on charging has been determined, by magnetometry; it is in good agreement with the quantity of charge passed associated with the O-redox plateau, reinforcing the assignment of O-redox to O<sub>2</sub> formation. Mg<sup>2+</sup> is displaced into tetrahedral and octahedral sites in the alkali metal layers, with equal amounts of Mg<sup>2+</sup> in each, and enables the Mn in-plane disordering in the transition metal layers generating vacancy cluster voids that accommodate O<sub>2</sub> molecules. On discharge, partial reformation of the honeycomb ordering occurs as seen in neutron-PDF and consistent with a partial plateau on the 2<sup>nd</sup> charge. The occupancy of tetrahedral sites on charge and

the partial reformation of honeycomb ordering on discharge make the divalent cation O-redox distinct from their monovalent counterparts.

### Resource Availability

*Lead contact* - Further information and requests for resources and reagents should be directed to and will be fulfilled by the lead contact, P.G.B. ([peter.bruce@materials.ox.ac.uk](mailto:peter.bruce@materials.ox.ac.uk)).

*Materials availability* - The materials in this study will be made available on request.

*Data and code availability* - Full experimental procedures are provided in the experimental section.

### Experimental

*Synthesis* –  $\text{Na}_{0.67}\text{Mn}_{0.72}\text{Mg}_{0.28}\text{O}_2$  was synthesized as described previously using  $\text{Na}_2\text{CO}_3$  ( $\geq 99.0\%$ , Aldrich),  $\text{MgO}$  ( $\geq 99.99\%$ , Aldrich) and  $\text{Mn}_2\text{O}_3$  ( $\geq 99.9\%$ , Aldrich) as precursors.<sup>10</sup> The material was transferred to an Ar-filled glove-box and stored under Ar without any exposure to air.

*Electrochemical measurements* - Electrodes were prepared by mixing 80 wt% active material, 10 wt% carbon black acetylene and 10 wt% polytetrafluoroethylene (PTFE) binder (in a mortar pestle and rolling out thin free standing films of the mixture). Electrochemical testing was carried out with Na metal-disk as anode and a 1M  $\text{NaPF}_6$  dissolved in EC:DEC solution electrolyte. Galvanostatic charge-discharge was carried out in coin cells using a Maccor Series 4000 at a rate of  $10 \text{ mAg}^{-1}$ . Except otherwise specified, the ex-situ samples were prepared by disassembling the coin cells under an inert argon atmosphere inside a glovebox ( $\text{O}_2$  and  $\text{H}_2\text{O} < 1 \text{ ppm}$ ) and the cathodes washed in dry dimethyl carbonate twice before being dried under vacuum.

*Neutron Powder Diffraction (NPD) and Neutron Pair Distribution Function (n-PDF)* - Neutron scattering was carried out on the POLARIS diffractometer (ISIS, UK) in Time-Of-Flight (TOF) mode in cylindrical 6 mm-diameter vanadium cans and measured for 7 h on approximately 1 g of powder. Rietveld analysis of NPD were carried out using the Fullprof software package.<sup>24</sup> The cycled samples have been prepared in 10 cm diameter electrochemical cell and without binder. The total scattering data have been extracted from NPD after correction for the effects of background scattering from the sample environment and beam attenuation using the program GudrunN.<sup>25</sup> The resultant normalized total scattering structure factors were Fourier transformed to obtain the corresponding total radial PDF which were analysed using PDF-GUI.<sup>26</sup> The relaxed structures obtained from DFT were used as starting model for the fits of n-PDF patterns. Only cell parameters, Scale factors, isotropic Debye-Waller factors and the correlated atomic motion factor were refined while atomic position, occupancies were fixed to that obtained from DFT. As the charged samples obtained from the cells

were composed of 35% of  $\text{P2-Na}_{0.54}\text{Mn}_{0.72}\text{Mg}_{0.28}\text{O}_2$  and 65% of  $\text{O2-Na}_0\text{Mn}_{0.72}\text{Mg}_{0.28}\text{O}_2$  (based on the capacity achieved under such conditions), multiphase refinements were employed.

*soft X-ray Absorption Spectroscopy (XAS) and Resonant Inelastic X-ray Scattering (RIXS)*– O K-edge XAS data have been collected on BL27SU (Spring8, Japan) and the high resolution O K-edge RIXS spectra were recorded at the ADRESS beamline (Swiss Light Source, PSI, Switzerland) using the SAXES spectrometer at an excitation energy of 531eV. The data were measured under  $10^{-6}$  Pa high-vacuum conditions excluding any contribution from surface adsorbed  $\text{O}_2$ .

*Magnetometry* - Magnetic data were collected on a Physical Property Measurement System (PPMS) Dynacool (9T) system from Quantum Design on *ca.* 20 mg of  $\text{Na}_x\text{Mn}_{0.72}\text{Mg}_{0.28}\text{O}_2$  electrodes. We performed measurements using zero field cooling (ZFC) procedures under a field of 500 Oe between 50 and 350 K. The Curie constants have been extracted from the  $1/\chi_{\text{mol}} = f(T)$  slope in the paramagnetic domain (100K-275K).

*Operando X-Ray Powder Diffraction (PXRD)* - Operando diffraction data were collected on a Rigaku 9kW SmartLab Cu-source diffractometer using a homemade electrochemical cell with a Be window.

*Extended X-ray Absorption Fine Structure (EXAFS)* – Mn K-edge EXAFS data were collected on B18 Core EXAFS beamline at Diamond Light Source (DLS, UK) while Mg K-edge EXAFS data have been collected on BL27SU (Spring8, Japan). Each spectrum were summed over 3 scans, calibrated, background subtracted, normalized and then the  $k^3$ -weighted EXAFS data have been extracted using the 1.5-11.5  $\text{\AA}^{-1}$   $k$ -range for Mn and 1.5-9.0  $\text{\AA}^{-1}$   $k$ -range for Mg with the Athena software<sup>27</sup>. The Fit of  $k^3$ -weighted Mg K-edge EXAFS has been performed in the  $R$ -range 1.0-3.2  $\text{\AA}$  using the lowest energy DFT structure as started model as described in the caption of **Table S3**.

*Density Functional Theory (DFT)* - Calculations were carried out using the Quantum Espresso suite.<sup>28,29</sup> The Perdew, Burke and Ernzerhof (PBE) exchange-correlation functional was employed.<sup>30</sup> The core-valence interaction was taken into account via the projector-augmented wave (PAW) method.<sup>31</sup> The wavefunctions and charge density were represented via plane-wave basis sets with energy cutoffs of 80 and 400 Ry, respectively. To correctly describe the energetics of the Mn 3d states, Hubbard corrections (DFT+U) were included, with  $U = 4$  eV. A  $2 \times 2 \times 3$  Monkhorst–Pack  $k$ -point grid was employed for sampling the Brillouin zone. Crystal structures were relaxed until forces on the atoms were less than 0.01 eV/Angstrom and total stresses on the cell were less than 0.04 kBar. A supercell of the closely related compound  $\text{P2-Na}_{2/3}\text{Mn}_{2/3}\text{Mg}_{1/3}\text{O}_2$ , containing 88 atoms (16 Na atoms; 16 Mn atoms;

8 Mg atoms; and 48 O atoms), was optimized and used as initial structure to investigate charge and discharge states. To investigate in-plane Mn and Mg disorder in the charge state, structural models with different orderings were prepared using combinatorics. Simple random sampling was used to choose a representative subset of non-symmetry equivalent configurations for relaxation. Fully desodiated models were considered to make calculations more computationally tractable. On the top of the DFT+U simulations, we performed hybrid calculations employing the Heyd–Scuseria–Ernzerhof (HSE) functional<sup>32</sup>, with an exact exchange mixing parameter of 0.25. For these specific calculations, norm-conserving pseudopotentials were used. The input structures were obtained from the DFT+U optimizations, and the atomic positions were allowed to further relax at the HSE level, with the lattice parameters fixed. A correction of 1.05 eV/O<sub>2</sub> was introduced in the calculation of formation energies, to remediate the overestimation of the binding energy of O<sub>2</sub> by the HSE functional in comparison with experiment.<sup>33,34</sup>

### **Acknowledgments**

P.G.B. is indebted to the EPSRC, the Henry Royce Institute for Advanced Materials (EP/R00661X/1, EP/S019367/1, EP/R010145/1), the Faraday Institution (FIRG007, FIRG008) as well as Shell for financial support and especially Dr. Peter Klusener (Senior process development chemist, Shell) for fruitful discussions. We acknowledge technical and experimental support at the B18 (DLS, UK) by Alan Chadwick and Gianntonio Cibirin, at BL27SU (Spring8, Japan) by Kazuki Tsuruta, at ADRESS (SLS, Switzerland) by Xingye Lu, Daniel McNally and Thorsten Schmitt, by Helen Playford and Ron Smith at POLARIS (ISIS, UK) and by Claire Minaud (UCCS, UMR-CNRS 8181, Université Lille-ENSCL, Villeneuve d'Ascq, France) for magnetometry data collection. We also acknowledge the resources provided by the Cambridge Tier-2 system operated by the University of Cambridge Research Computing Service (<http://www.hpc.cam.ac.uk>) funded by EPSRC Tier-2 capital grant (EP/P020259/1), via the BATDesign and AMAiB projects.

### **Author contributions**

E. B. conceived and conducted the experimental work with contributions from R.A.H, J.-J.M. U. M. and G.J.R. E.B. performed and analysed electrochemical tests, XAS, EXAFS, ND and n-PDF experiments. R.A.H collected operando XRD, XAS data, J.-J. M collected XAS and magnetometry data and U.M. collected RIXS data. M.A.P.-O. performed and interpreted the DFT calculations. EB, R.A.H. and P.G.B. wrote the manuscript with contributions from all the authors.

### **Declaration of Interests**

The authors declare no conflict of interests.

## References

1. Luo, K. *et al.* Charge-compensation in 3d-transition-metal-oxide intercalation cathodes through the generation of localized electron holes on oxygen. *Nat. Chem.* **8**, 684–691 (2016).
2. Gent, W. E. *et al.* Coupling Between Oxygen Redox and Cation Migration Explains Unusual Electrochemistry in Li-Rich Layered Oxides. *Nat. Commun.* **8**, 1–12 (2017).
3. Koga, H. *et al.* Different oxygen redox participation for bulk and surface : A possible global explanation for the cycling mechanism of  $\text{Li}_{1.20}\text{Mn}_{0.54}\text{Co}_{0.13}\text{Ni}_{0.13}\text{O}_2$ . *J. Power Sources* **236**, 250–258 (2013).
4. Seo, D.-H. *et al.* The structural and chemical origin of the oxygen redox activity in layered and cation-disordered Li-excess cathode materials. *Nat. Chem.* **8**, 692–7 (2016).
5. Hong, J. *et al.* Metal–oxygen decoordination stabilizes anion redox in Li-rich oxides. *Nat. Mater.* **18**, 256–265 (2019).
6. McCalla, E. *et al.* Visualization of O-O peroxo-like dimers in high-capacity layered oxides for Li-ion batteries. **350**, 1516–1521 (2015).
7. Chen, Z., Li, J. & Zeng, X. C. Unraveling Oxygen Evolution in Li-Rich Oxides: A Unified Modeling of the Intermediate Peroxo/Superoxo-like Dimers. *J. Am. Chem. Soc.* **141**, 10751–10759 (2019).
8. House, R. A. *et al.* Superstructure control of first-cycle voltage hysteresis in oxygen-redox cathodes. *Nature* **577**, 502–508 (2020).
9. House, R. A. *et al.* First cycle voltage hysteresis in Li-rich 3d cathodes associated with molecular  $\text{O}_2$  trapped in the bulk. *Nat. Energy* **5**, 777–785 (2020).
10. Maitra, U. *et al.* Oxygen redox chemistry without excess alkali-metal ions in  $\text{Na}_{2/3}[\text{Mg}_{0.28}\text{Mn}_{0.72}]\text{O}_2$ . *Nat. Chem.* **10**, 288–295 (2018).
11. Bai, X. *et al.* Anionic Redox Activity in a Newly Zn-Doped Sodium Layered Oxide  $\text{P2-Na}_{2/3}\text{Mn}_{1-y}\text{Zn}_y\text{O}_2$  ( $0 < y < 0.23$ ). *Adv. Energy Mater.* **8**, (2018).
12. Sathiya, M. *et al.* Origin of voltage decay in high-capacity layered oxide electrodes. *Nat. Mater.* **14**, 230–238 (2015).
13. Song, B. *et al.* A novel P3-type  $\text{Na}_{2/3}\text{Mg}_{1/3}\text{Mn}_{2/3}\text{O}_2$  as high capacity sodium-ion cathode using reversible oxygen redox. *J. Mater. Chem. A* **7**, 1491–1498 (2019).
14. Wang, Y. *et al.* Ultralow-Strain Zn-Substituted Layered Oxide Cathode with Suppressed P2–O<sub>2</sub> Transition for Stable Sodium Ion Storage. *Adv. Funct. Mater.* **30**, 1–9 (2020).
15. Århammar, C. *et al.* Unveiling the complex electronic structure of amorphous metal oxides. *Proc. Natl. Acad. Sci. U. S. A.* **108**, 6355–6360 (2011).
16. Rubensson, J. E., Pietzsch, A. & Hennies, F. Vibrationally resolved resonant inelastic soft X-ray scattering spectra of free molecules. *J. Electron Spectros. Relat. Phenomena* **185**, 294–300 (2012).
17. Radjenovic, P. M. & Hardwick, L. J. Evaluating chemical bonding in dioxides for the development of metal-oxygen batteries: Vibrational spectroscopic trends of dioxygenyls, dioxygen, superoxides and peroxides. *Phys. Chem. Chem. Phys.* **21**, 1552–1563 (2019).
18. Li, X. *et al.* Direct Visualization of the Reversible  $\text{O}_2^-/\text{O}^-$  Redox Process in Li-Rich Cathode Materials. *Adv. Mater.* **30**, 2–7 (2018).
19. Qiao, Y. *et al.* Reversible anionic redox activity in  $\text{Na}_3\text{RuO}_4$  cathodes: A prototype Na-rich layered oxide. *Energy Environ. Sci.* **11**, 299–305 (2018).
20. Yabuuchi, N. *et al.* A new electrode material for rechargeable sodium batteries: P2-type  $\text{Na}_{2/3}[\text{Mg}_{0.28}\text{Mn}_{0.72}]\text{O}_2$  with anomalously high reversible capacity. *J. Mater. Chem. A* **2**, 16851–16855 (2014).
21. Hellenbrandt, M. The inorganic crystal structure database (ICSD) - Present and future. *Crystallogr. Rev.* **10**, 17–22 (2004).
22. Dai, K. *et al.* High Reversibility of Lattice Oxygen Redox Quantified by Direct Bulk Probes of Both Anionic and Cationic Redox Reactions. *Joule* **3**, 518–541 (2019).
23. Wu, J. *et al.* Dissociate lattice oxygen redox reactions from capacity and voltage drops of

- battery electrodes. *Sci. Adv.* **6**, 1–12 (2020).
24. Rodriguez-carvajal, J. recent advances in magnetic structure determination by neutron powder diffraction. *Phys. B* **192**, 55–69 (1993).
  25. Soper, A. K. GudrunN and GudrunX: Programs for Correcting Raw Neutron and X-ray Diffraction Data to Differential Scattering Cross Section. (2011).
  26. Juhás, P., Louwen, J. N., van Eijck, L., Vogt, E. T. C. & Billinge, S. J. L. PDFgetN3: Atomic pair distribution functions from neutron powder diffraction data using ad hoc corrections. *J. Appl. Crystallogr.* **51**, 1492–1497 (2018).
  27. Ravel, B. & Newville, M. ATHENA, ARTEMIS, HEPHAESTUS: data analysis for X-ray absorption spectroscopy using IFEFFIT. *J. Synchrotron Radiat.* **12**, 537–541 (2005).
  28. Giannozzi, P. *et al.* QUANTUM ESPRESSO : a modular and open-source software project for quantum simulations of materials. *J. Phys. Condens. Matter* **21**, (2009).
  29. Cococcioni, M. & Gironcoli, S. De. Linear response approach to the calculation of the effective interaction parameters in the LDA+U method. *Phys. Rev. B* **71**, 1–16 (2005).
  30. Perdew, J. P., Burke, K. & Ernzerhof, M. Generalized Gradient Approximation Made Simple. *Phys. Rev. Lett.* **77**, 3865–3868 (1996).
  31. Bloch, P. E. Projector augmented-wave method. *Phys. Rev. B* **50**, 17954–17979 (1994).
  32. Heyd, J. *et al.* Hybrid functionals based on a screened Coulomb potential. *J. Chem. Phys.* **118**, 8207–8215 (2003).
  33. Wang, L., Maxisch, T. & Ceder, G. Oxidation energies of transition metal oxides within the GGA+U framework. *Phys. Rev. B - Condens. Matter Mater. Phys.* **73**, 1–6 (2006).
  34. Kang, S., Mo, Y., Ong, S. P. & Ceder, G. A facile mechanism for recharging Li<sub>2</sub>O<sub>2</sub> in Li-O<sub>2</sub> batteries. *Chem. Mater.* **25**, 3328–3336 (2013).